RESEARCH ARTICLE

Nanophotocatalytic Desulfurization of Hydrophane 10 Base Oil of Tehran Refinery

Mojgan Jalali Farahani[1], Reza Fazaeli[2]*, Ensieh Ghasemi[1]

[1] Department of Chemistry Department, Pharmaceutical Sciences Branch, Islamic Azad University (IAUPS), Tehran, Iran

[2] Department of Chemistry, South Tehran Branch, Islamic Azad University, Tehran, Iran

ARTICLE INFO

Article History:
Received 19 Sep 2019
Accepted 27 Nov 2019
Published 1 Feb 2020

Keywords:
DOE
Ni(8%)TiO$_2$/Zeolite NaX
Photocatalyst
Sulfur Pollutants
Zeolite

ABSTRACT

In this research, Ni(8%)/TiO$_2$/Zeolite NaX nanophotocatalyst was synthesized and evaluated as a desulfurizer catalyst from hydrophane 10 base oil. Various tests, including X-ray diffraction (XRD), Scanning Electron Microscopy (SEM), Energy-Dispersive X-ray Analysis (EDXA), Transmission Electron Microscopy (TEM), Atomic Force Microscopy (AFM), and BET/BJH were used to evaluate the photocatalyst synthesis process. Initially, using Design of Experiment (DOE) technique, optimum influential parameters were predicted, and 2D plus 3D diagrams were plotted. Then, 50 ml of oil containing 3782 ppm total sulfur, 0.6 g catalyst, 0.8 g adsorbent, and 3 h contact time were able to remove 20% of sulfur when exposed to the visible light. Sulfur was measured at all steps using inductively coupled plasma (ICP) technique. The final results suggested that the nanophotocatalytic process is a feasible way when compared to difficult and complicated steps with harder conditions.

How to cite this article
Jalali Farahani M, Fazaeli R, Ghasemi E. Nanophotocatalytic Desulfurization of Hydrophane 10 Base Oil of Tehran Refinery. J. Nanoanalysis., 2020; 7(1): 10-20. DOI: .

INTRODUCTION

Environmental concerns have led to increasing attention to fuel and other refinery products in recent years. SO_X and NO_X are released from air pollution sources and acidic rain which are produced during the combustion process. Along with all these hazards, corrosion of engine parts and the toxicity of consuming catalysts are also important [1-2]. Sulfur-containing compounds are one of the most important oil pollutants. Environmental pollutions, because of hazards to human health, corrosion in pipelines, and other refinery and installments necessitate sulfur removal [6].

Hydrodesulfurization (HDS) is a catalytic reaction applied for elimination of sulfides and disulfides as well as thiophanes. This method needs high temperatures and a great amount of hydrogen and yet has a low efficiency for massive compounds such as dibenzotiophen. Therefore, finding new alternatives such as bio-desulfurization and selective adsorption, and extraction by ionic liquids have been introduced which have led to deep desulfurization during the process [8,16].

Meanwhile, photocatalytic oxidation shows almost a good performance in sulfur removal from oils and fuels under mild conditions. Low-cost investment and efficient sulfur removal via this technology are considerable [5-7]. Thus, the photocatalytic strategy has been introduced as one of the advanced solutions in sulfur removal. Many photocatalysts have been mentioned for their excellent performance in sulfur catalytic oxidation such as photocatalyst-based semiconductors [3-9]. Extractive and catalytic oxidative desulfurization (ECODS) has been considered as one of the major oxidative desulfurization (ODS) methods thanks to its unique conditions such as high thermal resistance and good solubility [19-20].

Meanwhile, titanium dioxide is a non-polluting and inexpensive semiconductor. Researchers

* Corresponding Author Email: r_fazaeli@azad.ac.ir

have extensively studied TiO_2 and its effects on nanotubes morphology as carriers [4].

The amount of hydrodesulfurization is strongly bound to the structure of the sulfur compound [10,16,18]. Desulfurization of fuel oils for petrochemical industry is attracting a great deal of attention. Many areas have extreme sulfur limitations in fuel compounds; for example, sulfur in gasoline and diesel fuel in China has reached less than 10 μg/g [11]. Hence, many scientists are trying to develop desulfurization process with a higher performance and milder conditions.

Sulfur removal from petroleum products is an important step in many processes. Since a very small degree of sulfur contamination could poisoned catalysts and reduce their useful life, so far, several advanced and cost-effective techniques have been developed to overcome the limitations including hydrodesulfurization or adsorption. Indeed, the most commonly used desulfurization method in industries is hydrodesulfurization. However, this method requires high temperature, pressure, and a large amount of catalyst [12,15,17].

Selection of an adsorbent has a great influence on the efficiency of sulfur removal. Metal oxides are one of the most popular adsorbents and are used for working at extremely high temperatures. Different oxides of metals such as Zn, Mn, Cu, Co, Ni, Cr, Ca, and Fe are reported metal oxides utilized by researchers as absorbent in several experiments [7,12,13].

All of the techniques such as hydrodesulfurization (HDS), oxidation desulfurization (ODS), adsorption, extraction, sedimentation, etc. may be effective for the sulfur removal from heavy oil. Nevertheless, the ultimate goal is achieving proper efficiency with regards to the physical properties such as high viscosity and high sulfur-content [13-15].

EXPERIMENTAL SECTION

Chemicals

Sodium aluminate ($NaAlO_2$), fumed silica (SiO_2), sodium hydroxide (NaOH), hydrogen peroxide (H_2O_2), pure ethanol 99% (C_2H_5OH), titanium tetraisopropoxide (TTIP), nickel nitrate ($Ni(NO_3)_2.6H_2O$), and 1-Propanol (C_3H_8O) were purchased from Sigma Aldrich Company.

Instruments

The instruments included analytical Scale (accuracy 0.1 mg), centrifuge (NF1200) model Universal 320, digital furnace with adjustable temperature (Lenton Thermal Designs), vacuum oven (Vacuum Drying Oven), double beam UV-Visible, vacuum pump and Buchner funnel, desiccators, magnetic stirrer, water bath with adjustable temperature, photochemical reactor with Phillips Xenon lamp (400 Watt-visible).

Synthesis of Nano Zeolite Fujasite NaX

First, 5.34 g of sodium hydroxide was mixed with 2.42 g of sodium aluminate and further with 50 ml of distilled water stirred by a magnetic stirrer at 900 rpm for 1 h. Then, 3.43 g of fumed silica was added to this solution. After mixing for a few minutes, the prepared alumina silicate gel was transferred to a water bath with adjustable temperature. Mixing was continued for 4 days at the constant temperature of 60 °C. Then, this solution was centrifuged at 8,000 rpm for 20 min and washed, and the precipitate was purified by water and alcohol several times until the pH of the solution reached below 8. The precipitate was then placed in desiccators at room temperature for 24 h to dry and achieve further crystallization. For the calcination step, the precipitate was placed in a furnace with the following temperature program: 180 °C for 1 h, 250 °C for 2 h, 450 °C for 2 h, and 550 °C for 1 h.

Synthesis of Ni (8%)/TiO_2 /Zeolite NaX Nanophotocatalyst

The synthetic photocatalyst included nickel 8% on TiO_2 and loaded on an optimized amount of synthetic NaX nanozeolite. First, 0.785 g of $Ni(NO_3)_2.6H_2O$ was dissolved in 10 mL of deionized water without heating. Then, 90 mL of 1-propanol solvent was added dropwise and stirred for 1 h until a homogenous solution was obtained. At the third step, 10 mL of TTIP was injected dropwise carefully. This solution was stirred continuously without heating for 5 h.

In the next step, 4 g of dry NaX nanozeolite was mixed with ethanol 99%. Then, the solution prepared in the first step was injected dropwise carefully to this solution, while being stirred. The final solution was stirred without heating for 24 h.

This solution was transferred to a centrifuge (8,000 rpm) to be centrifuged for 30 min. The precipitate was washed with an equal amount of water/ethanol mixture several times. The catalyst was heated in the vacuum oven for 1 h at 80 °C and 4 h at 150 °C to evaporate organic wastes. Once dried, the sample was placed in the furnace at 150

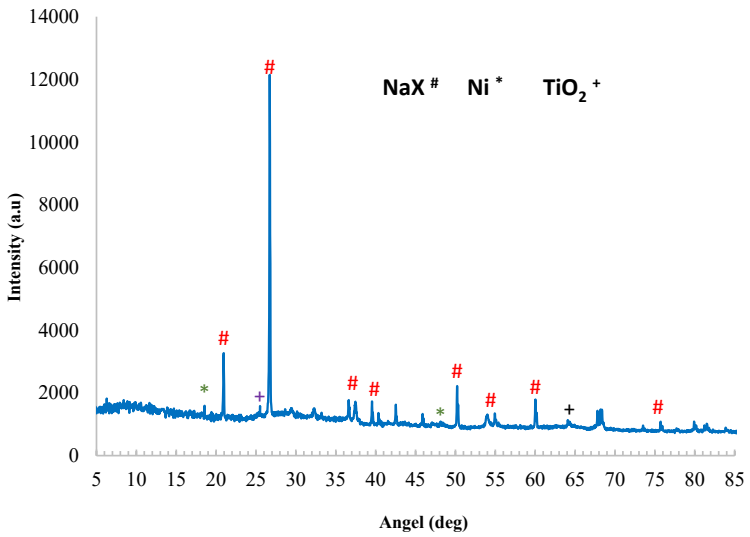

Fig. 1. X-rays pattern of TiO_2 and Ni loaded on NaX Zeolite

°C for 15 min, 250 °C for 30 min, 350 °C for 1 h, 450 °C for 2 h, 550 °C for 1 h, 650 °C for 30 min, and 750 °C for 30 min in order to accomplish calcinations. The resulting catalyst was ground to achieve a higher mesh in the form of Ni(8%)/TiO_2/Zeolite Na) nanoparticles as a light yellow solid powder. Finally, SEM analysis was performed for examining the morphology of the TiO_2 nanoparticles loaded on NaX. EDXA was performed for all the elements of the sample and for determining their weight percentages. The AFM analysis was conducted to study the morphology of the surface of the nanophotocatalyst. Further, BET/BJH was utilized to investigate the pore distribution of nanophotocatalyst before and after desulfurization. Also, XRD was employed to obtain information such as the size of the crystallites and heterogeneity of solid molecules. Finally, TEM imaging was performed to determine the substructures and the morphology of Ni(8%)/TiO_2/Zeolite NaX.

Characterization of Ni(8%)/TiO_2/Zeolite NaX)

As demonstrated in Fig. 1, there are many peaks for the catalyst of interest with different angles and intensities.

For identification and morphological investigation of TiO_2 and Ni loaded on NaX Zeolite nanoparticles' surfaces, SEM imaging was conducted, with the results displayed in Figs. 2 and 3.

As shown in Fig. 4, Ni and TiO nanoparticles loaded on Zeolite NaX are clearly observable. Further, the presence of Ca, Ni, O, Ti, Al, Na, and Si elements in the catalyst is approved via EDXA analysis.

Analysis of the elements based on the results of EDX

Element	Series	unn. C [wt.-%]	norm. C [wt.-%]	Atom. C [at.-%]
Oxygen	K series	53.89	51.10	70.12
Sodium	K series	0.00	0.00	0.00
Magnesium	K series	0.84	0.76	0.69
Aluminium	K series	0.59	0.54	0.44
Silicon	K series	19.34	19.51	15.25
Calcium	K series	5.65	9.17	5.02
Titanium	K series	17.13	16.58	7.60
Nickel	K series	2.56	2.34	0.88
		100	100	100

Total: 100.0 %

According to the TEM results, nickel particles loaded on NAX nanozeolite are observable as dark points in the figures.

To examine the surface changes before and after abrasion in nano dimensions, the AFM technique was used. As displayed in Fig. 6, surface abrasion is considerable in the Ni(8%)/TiO_2/Zeolite NaX zeolite during photocatalytic reaction.

Based on Fig. 7, the result of BET/BJH analysis for the mentioned catalyst can be used to justify the hysteresis and shapes of capillaries before and after the catalytic reaction.

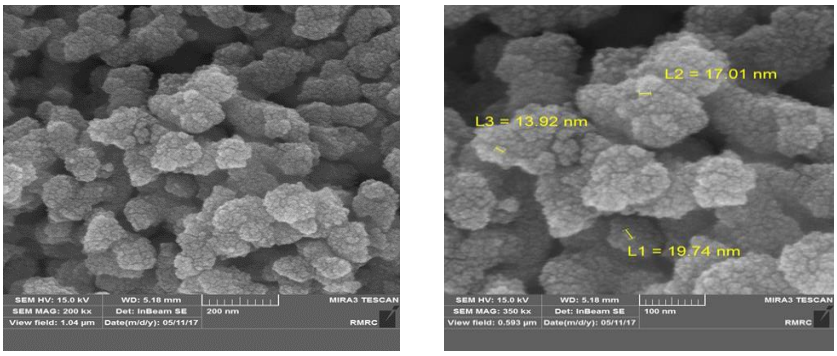

(a) (b)

Fig. 2. SEM image of nanophotocatalyst particles Ni(8%)/ TiO_2 /Zeolite NaX with resolutions of 100 nm and 200 nm

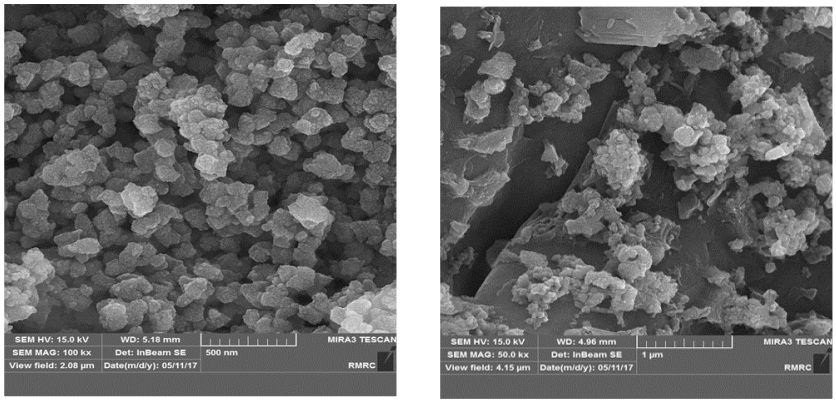

(c) (d)

Fig. 3. SEM image of nanophotocatalyst particles Ni(8%)/ TiO_2 /Zeolite NaX with resolutions 500 nm (c) and 1μm (d)

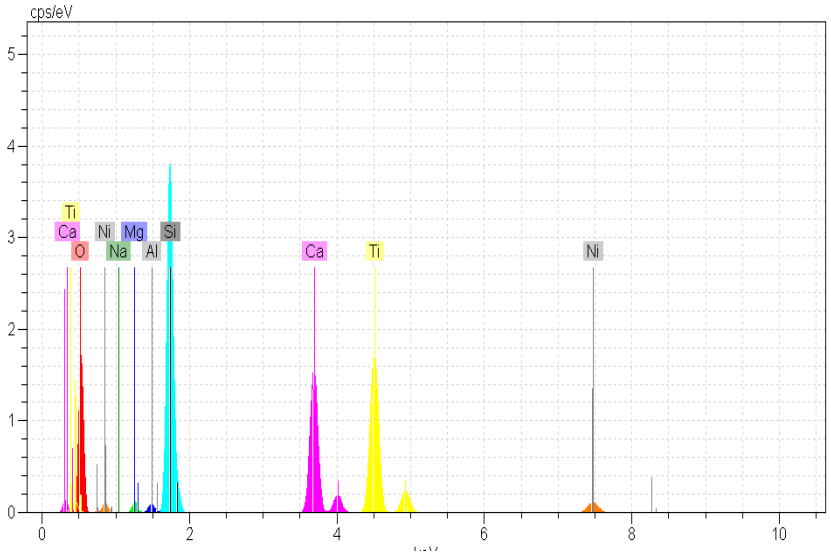

Fig. 4. EDXA results for Ni and TiO2 loaded on Zeolite NaX

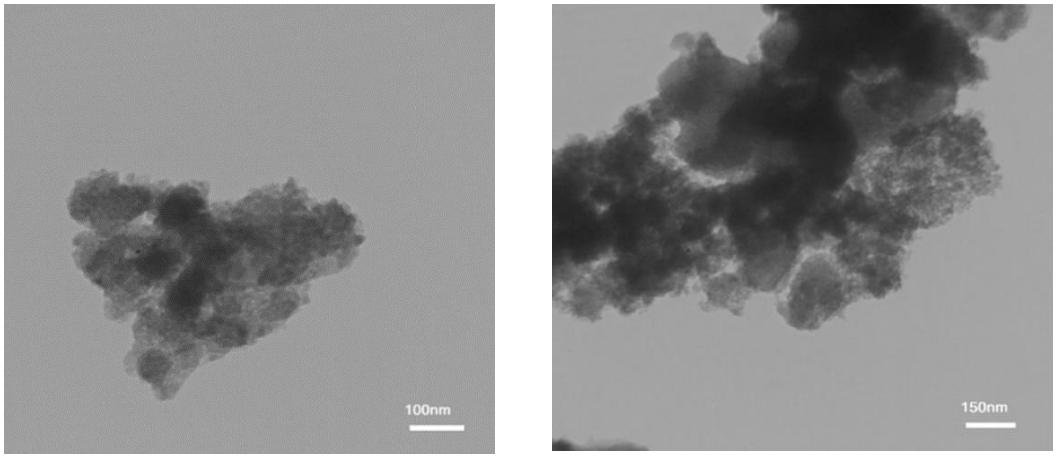

Fig. 5. TEM image of the nanophotocatalyst

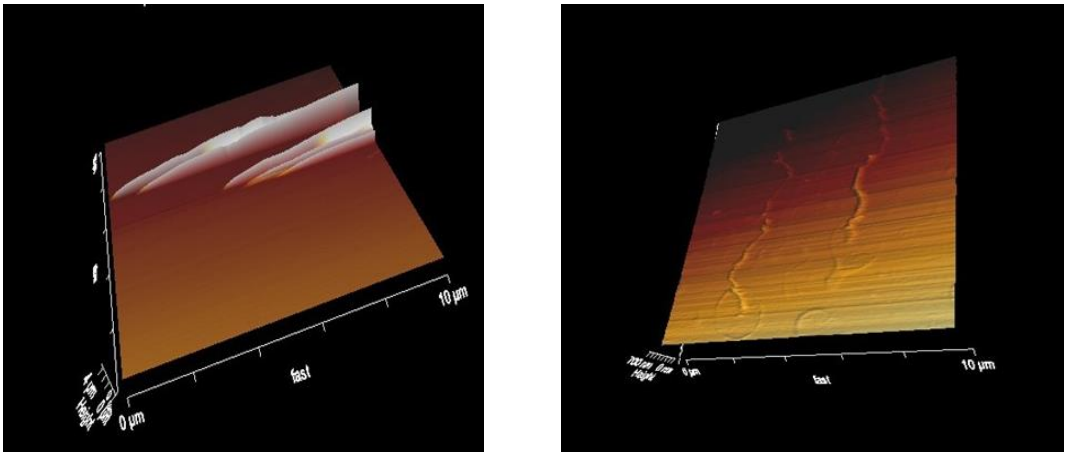

Fig. 6. AFM images of nanophotocatalyst Ni(8%)/TiO_2/Zeolite NaX before (a) and after (b) desulfurization

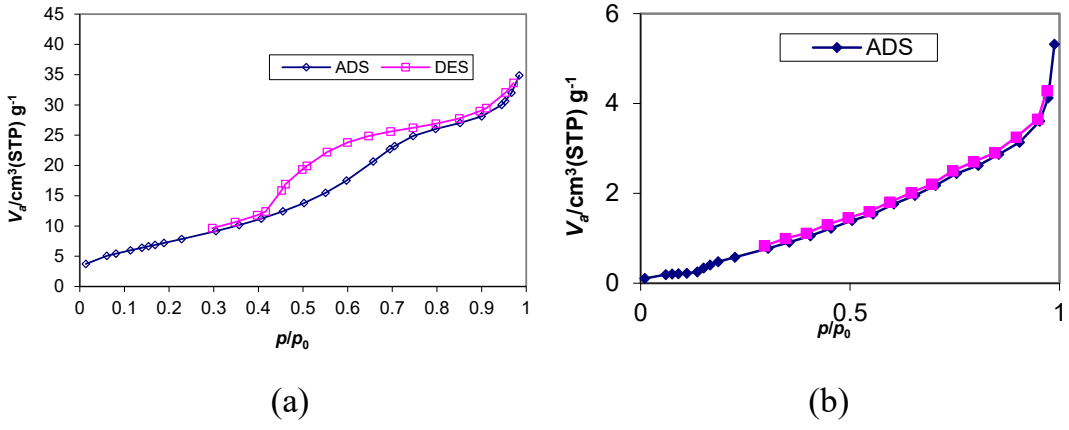

Fig. 7. Hysteresis loop before (a) and after (b) desulfurization by the nanophotocatalyst

Table 1. Photocatalytic Reaction Conditions

No.	adsorbent mass (g)	catalyst mass (g)	contact time (h)
1	0.7	0.9	2
2	0.7	0.9	6
3	0.5	0.9	4
4	0.9	0.9	4
5	0.7	0.7	4
6	0.7	0.7	4
7	0.7	0.7	4
8	0.5	0.7	6
9	0.5	0.7	2
10	0.9	0.7	6
11	0.9	0.7	2
12	0.7	0.5	6
13	0.7	0.5	2
14	0.5	0.5	4
15	0.9	0.5	4

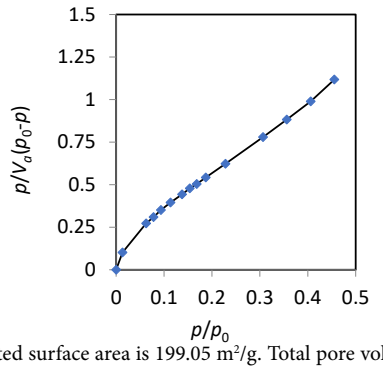

Fig. 8. BET plot for NaX zeolite. The calculated surface area is 199.05 m^2/g. Total pore volume (in p/p^0=0.982) is 0.007922 cm^3/g and the average pore diameter is 15.92 nm

Photocatalytic Reaction Conditions

Based on experimental Design procedure, the Hydrfan 10 engine oil was applied in 15 experiments that shown in Table 1.

Design of Experiment

Design Expert 7 software was used to the calculate the parameters affecting the process. The response surface methodology (RSM) was utilized as follows:

$$Y = \beta_0 + \sum_{j=1}^{k} \beta_j X_j + \sum_{j=1}^{k} \beta_j X_j^2 + \sum_{i} \sum_{<j=2}^{k} \beta_i X_i X_j + e_i$$

According to ANOVA results, the statistical coefficients show that the model is significant. In this study, the effects of independent variables X_1 (catalyst mass), X_2 (adsorbent mass) and X_3 (time) were evaluated in three levels.

The transfer function according to the dependent variable in Fig. 9 demonstrates that the data are normal and follow a normal distribution.

It is noticeable that even with normal data, average dispersion is expected. Curved patterns are easily recognizable and better analysis could be reached by a transfer function on the dependent variable or model answer.

The residual values versus time is indicated in Fig. 10, indicating that the desired factor is independent of time. Further, its condition, from a mean and variance perspective, does not change in an organized way over time.

Fig. 11 illustrates the internally studentizied residuals against predicted values of the response, and tests the assumption of the constant variable.

The graph should have a random distribution which shows a fixed pattern throughout the graph. Patterns with larger signs need a power transfer function. In this graph, the data should not deviate

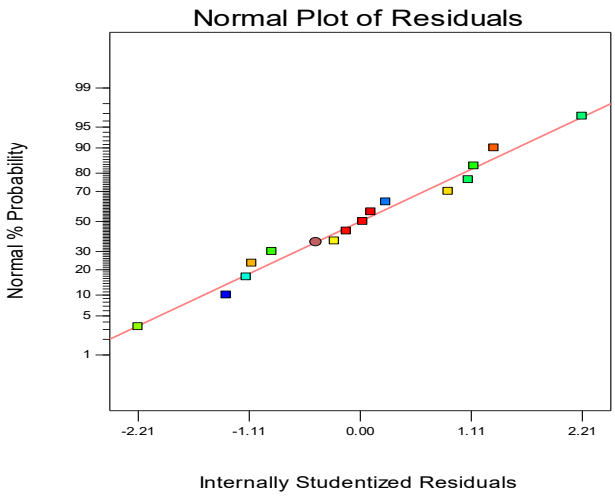

Fig. 9. Transfer functions according to the dependent variable

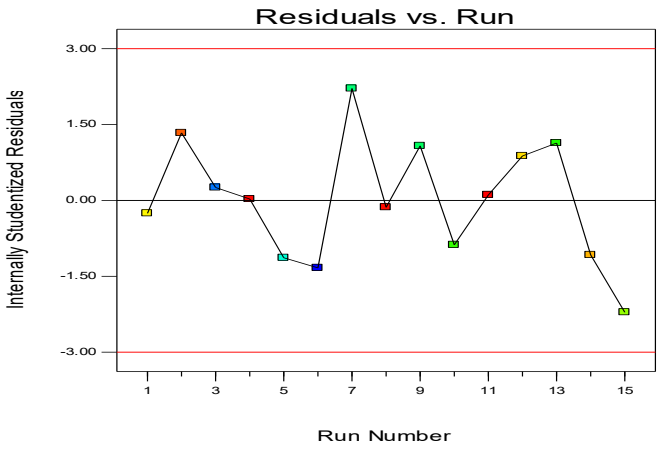

Fig. 10. The residual values over time

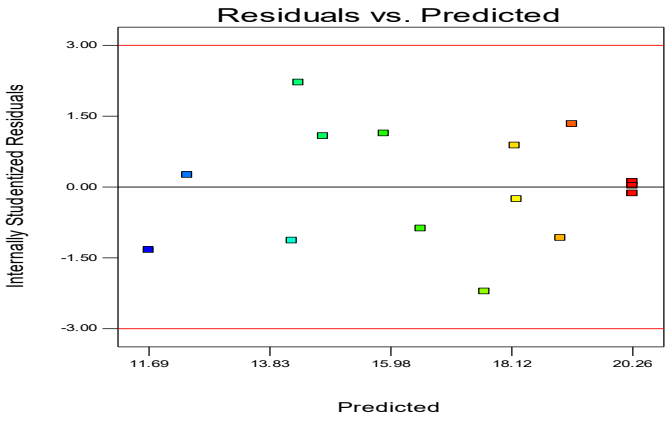

Fig. 11. The internally studentizied residuals according to the predicted values

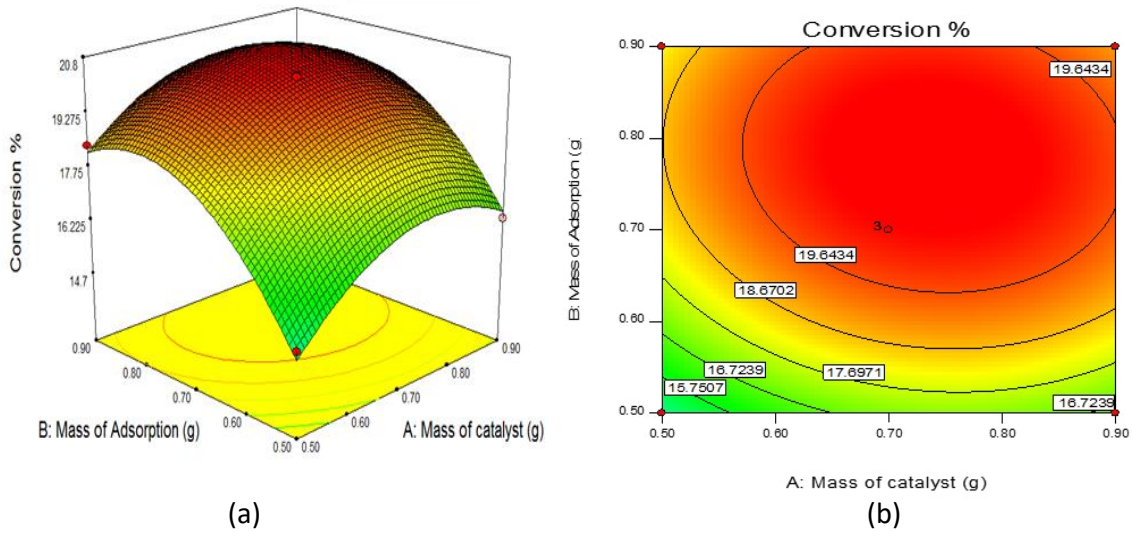

Fig. 12. The changes in conversion percentage relative to the catalyst mass and adsorbent mass in 2D and 3D formats

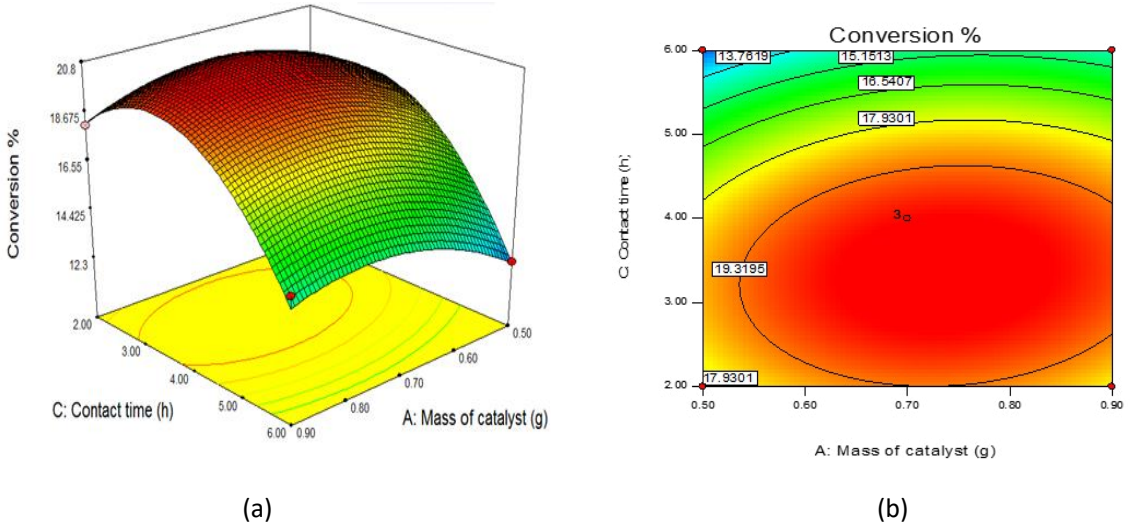

Fig. 13. The changes of conversion percentage relative to the catalyst mass and contact time in 2D and 3D formats

from the determined limits. This condition has been established here.

Reviewing and analyzing different parameters in 2D and 3D graphs

The effect of the catalyst mass and the adsorbent mass

Fig. 12 demonstrates the effect of catalyst mass and adsorbent mass and their interactions in the catalytic desulfurization process in the form of 2D and 3D graphs.

The high efficiency for the catalyst mass and adsorbent mass have been 0.65 g and 0.70 g, respectively. Therefore, the adsorbent mass parameter is more effective than the catalyst mass, and contributes to the optimum desulfurization level of 16.72%.

The Effect of Catalyst Mass and the Contact Time

The effect of catalyst mass and the contact time and their interactions in the desulfurization process as 2D and 3D graphs is displayed in Fig. 13.

The high efficiency for the catalyst mass and contact time have been 0.65 g and 3.5 h, respectively. Therefore, the contact time parameter is more effective than the catalyst mass parameter

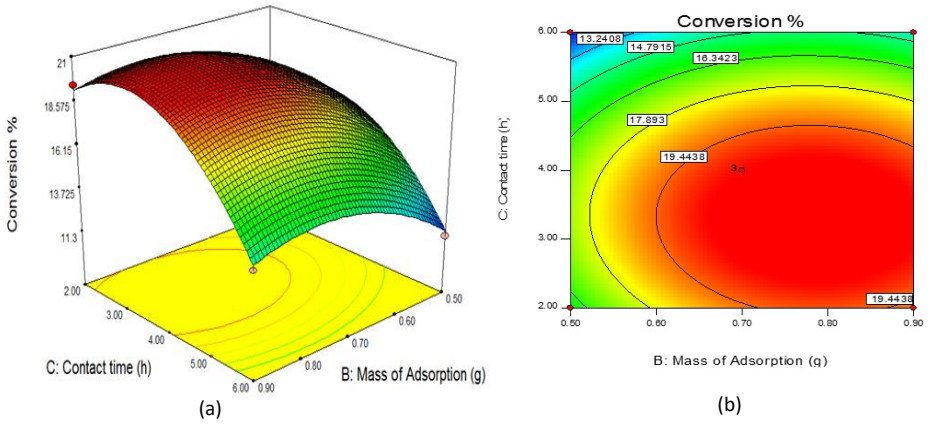

Fig. 14. The changes in conversion percentage relative to the absorbent mass and contact time in 2D and 3D formats

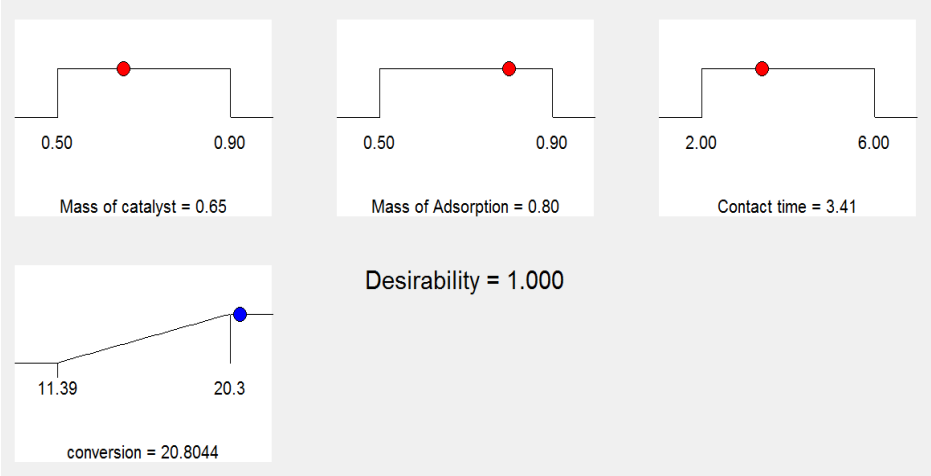

Fig. 15. Determining the optimum conditions in the desulfurization process of hydrophane 10 oil

and contributes to the optimum desulfurization magnitude of 17.93%.

The Effect of the adsorbent Mass and the contact time

As shown in Fig. 14, the highest efficiency for the adsorbent mass and contact time have been 0.7 g and 3.5 h, respectively. Therefore, the contact time parameter is more effective than the adsorbent mass parameter and contributes to the optimum desulfurization value of 19.44%.

Process optimization

As observed in Fig. 15, the software showed that three effective factors, including catalyst mass (0.6 g), adsorbent mass (0.8 g), and contact time (3.41 h), resulted in the highest optimum desulfurization (20%).

CONCLUSION

The results of XRD analysis, after calcination according to a specific temperature programming, are presented in Fig. 1. Based on interpretation with X'pert software, the crystalline structure is tetragonal. Crystal faces (101), (103), (111), (105), and (215) were observed in the zones 25.34°, 37.91°, 47.84°, 54.965°, and 75.35°, respectively. A remarkable point is the presence of metal nickel peak with crystal face (111) at 47.84 ° as well as widening and weakening of titaniumdioxide peaks, which can be due to either the formation of particles on its surface or changes in the morphology. Further, wide peaks with less intensity in the diffractogram can be due to the low loading rate of nickel oxide in the catalyst and formation of very small particles with high or none accessible distribution on the base.

Table 2. linear regression equation coefficient and ANOVA results

Std.Dev	0.45	R^2	0.9912
Mean	16.85	Adj R^2	0.9715
C.V%	2.67	Pred R^2	0.8602
PRESS	16.13	Adeq Precision	0.23336

Table 3, The results of BET/BJH

Catalyst	multi point BET (m^2/g)	total pore volume for pores (mL/g)	micropore volume (mL/g)	Average pore diameter (nm)
(Ni(8%)/TiO_2/Zeolite NaX)	73.48	0.164	0.038	8.905

Also, according to the results of XRD analysis, the average size of photocatalyst particles according to Debye-Scherer equation was estimated to be 50.9 nm. Eventually, the crystallinity of the photocatalyst particles was estimated to be above 95%.

FESEM technique was used in order to identify the morphology of the surface of photocatalyst nanoparticles. The results of the images taken from photocatalyst are revealed in Figs. 2 and 3, in which the particles have formed a cluster. The lighter parts belong to Ni metal, showing it as doped very well on TiO_2. Also, we used microstructure measurement software to determine the particle size. The average sizes of the particles in Figs. 2 and 3 are 89.90 and 50.36 nm, respectively. Additionally, in order to calculate the percentage distribution of nickel particles doped on the catalyst surface, Image analyzer software was employed. According to the results, the average particle distributions of Ni metal on the catalyst surface in Figs. 1 and 2 are 8.47% and 8.40%, respectively.

The TEM images of the photocatalyst are displayed in Fig. 5. Spherical nanotitania and nickel particles distributed on the zeolite bed are easily identifiable.

Some obstacles and limitations existed when taking AFM images since the sample was in the form of powder. As exhibited in Fig. 6, some roughness of the nanophotocatalyst surface is due to erosion, which reveals high mechanical erosion in the system.

BET and BJH tests were performed to determine the catalyst surface area and the average pore diameter as well as the volumes of the pores. Adsorption and desorption of nitrogen affect the characteristics of the porous structure. The main results of BET/ BJH are presented in Table 3. Note that due to doping nickel precursor, the catalyst surface was reduced in comparison to the base, owing to blockage of some base pores by nickel oxide following catalyst calcination.

The hysteresis loop of the catalyst, Fig. 7a, is consistent with the hysteresis loop type (D). A rise in the diameter of the pores up to 15 nm will result in increased volume. In response to the heightened diameter of the pores beyond 20 nm, the volume remained fixed at a gentle slope. According to the calculations, pores are mainly mesopores.

The results obtained after desulfurization showed no hysteresis loop. Cylindrical capillaries, closed at one end, did not show any hysteresis because the pores and bores did not postpone the liquid surface formation in the adsorption. According to Fig. 7b, the adsorption and desorption branches are superimposed; therefore, following the reaction, a major part of the catalyst pores are blocked. As a result, a large portion of pores with two open ends are filled, culminating in hysteresis loss.

In this study, removal of sulfur pollutants from base oils by nanophotocatalyst Ni(8%)/ TiO_2/Zeolite NaX was analyzed under visible light irradiation at different conditions and quantities. It was observed that 1 g of the adsorbent and 1 g of the catalyst could eliminate 4.72 g and 12.61 g of sulfur, respectively, indicating the considerable effect of catalyzing surface adsorption processes.

CONFLICT OF INTEREST

The authors declare that there is no conflict of interests regarding the publication of this manuscript.

REFERENCES

1. Gautham P. Jeppua , T. Prabhakar Clement. A modified Langmuir-Freundlich isotherm model for simulating pH-dependent adsorption effects. Journal of Contaminant Hydrology. 2012, 46(53):129–130.
2. Amin Bazyari, Abbas A. Khodadadi, Alireza Haghighat,

Mamaghani Javad Beheshtian, Levi T. Thompson, Yadollah Mortazavi. Microporous titania-silica nanocompositecatalyst-adsorbent for ultra-deep oxidative desulfurization (in press).
3. Si-Wen Li, Ying-Ying Li, Fei Yang , Zhe Liu, Rui-Min Gao, Jian-she Zhao. Photocatalytic oxidation desulfurization of model diesel over phthalocyanine/$La_{0.8}Ce_{0.2}NiO_3$, Journal of Colloid and Interface Science. 2015, 8(17):460.
4. Dan Zheng, Wenshuai Zhu, Suhang Xun, Miaomiao Zhou, Ming Zhang, Wei Jiang, Yuejiao Qin, Huaming Li. Deep oxidative desulfurization of dibenzothiophene using low-temperature-mediated titanium dioxide catalyst in ionic liquids. Fuel. 2015, 159:446–453.
5. Suzan Khayyat, L.Selva Roselin. Photocatalytic degradation of benzothiophene and dibenzothiophene using supported gold nanoparticle (in press).
6. Ezzat Rafiee, Mohammad Joshaghani, Parvaneh Ghaderi-Shekhi Abadi. Oxidative desulfurization of diesel by potato based-carbon as green support for $H_5PMo_{10}V_2O_{40}$: Efficient composite nanorod catalyst (in press).
7. XU Cheng-zhi, ZHENG Mei-qin, CHEN Keng, HU Hui, CHEN Xiao-hui. CeOx doping on a TiO_2-SiO_2 supporter enhances Ag based adsorptive desulfurization for diesel. Fuel Chemistry and Technology. 2016, 44(8):943–953.
8. Daniela Plana, David J. Ferm´ın. Photoelectrochemical activity of colloidal TiO_2 nanostructures assembled at polarisable liquid/liquid interfaces (in press).
9. Diana Rakhmawaty Eddy, Farisa Novita Puri, Atiek Rostika Noviyanti. Synthesis and Photocatalytic Activity of Silica-based Sand Quartz as the Supporting TiO_2 Photocatalyst. Procedia Chemistry. 2015, 17:55–58.
10. Xiuwen Cheng, Xiujuan Yu, Zipeng Xing, Lisha Yang. Synthesis and characterization of N-doped TiO_2 and its enhanced visible-light photocatalytic activity (in press).
11. Sunil Kumar, N.S. Bajwa, B.S. Rana, S.M. Nanoti, MO. Garg. Desulfurization of gas oil using a distillation, extraction and hydrotreatingbased integrated process. Fuel. 2018, 220:754-762.
12. Du Yue, Jiaheng Lei, Yang Peng, Junsheng Li, Xiaodi Du. Three-dimensional ordered phosphotungstic acid/TiO_2 with superior catalytic activity for oxidative desulfurization. Fuel. 2018, 226:148-155.
13. Tawfik A. Saleh. Simultaneous adsorptive desulfurization of diesel fuel over bimetallic nanoparticles loaded on activated carbon. Journal of Cleaner Production (in press).
14. Hamdi A. Al-Jamimi, Sadam Al-Azani, Tawfik A. Saleh. Supervised machine learning techniques in the desulfurization of oil products for environmental protection (in press).
15. Emmanuel Rodríguez, Guillermo Félix, Jorge Ancheyta, Fernando Trejo. Modeling of hydrotreating catalyst deactivation for heavy oil hydrocarbons. Feul. 2018, 225:118-133.
16. Yan Gao, Ziyan Lv, Ruimin Gao, Gai Zhang, Ying Zheng, Jianshe Zhao. Oxidative desulfurization process of model fuel under molecular oxygen by polyoxometalate loaded in hybrid material CNTs@MOF-199 as catalyst (in press).
17. Xiaoming Gao, Jiao Fei, Yanyan Shang, Feng Fu. Desulfurization of liquid hydrocarbon fuels via Cu_2O catalyzed photo-oxidation coupled with liquid–liquid extraction (in press).
18. Diana Julia˜o, Ana C. Gomes, Martyn Pillinger, Rita Valenc¸a, Jorge C. Ribeiro, Isabel S. Gonc¸alves, Salete S. Balula. Desulfurization of liquid fuels by extraction and sulfoxidation using H_2O_2 and [CpMo(CO)3R] as catalysts (in press).
19. M. Toghyani, A. Rahimi. UV-irradiation Effect on Desulfurization of Hydrocarbon Fuels through an Advanced Oxidation-Extraction Process in Presence of Acid Catalyst (in press).
20. Du Yue, Lei Jiaheng, Zhou Lina, Guo Zhen ran, Du Xiaodi, Li Junsheng. Highly efficient deep desulfurization of fuels by meso/macroporous $H_3PW_{12}O_{40}/TiO_2$ at room temperature. Materials Research Bulletin. 2018, 105:210–219.